

# Spontaneous gyrotropic electronic order in a transition-metal dichalcogenide

<https://doi.org/10.1038/s41586-020-2011-8>

Received: 24 September 2018

Accepted: 5 December 2019

Published online: 26 February 2020



Su-Yang Xu<sup>1,13</sup>, Qiong Ma<sup>1,13</sup>, Yang Gao<sup>2,13</sup>, Anshul Kogar<sup>1</sup>, Alfred Zong<sup>1</sup>, Andrés M. Mier Valdivia<sup>1</sup>, Thao H. Dinh<sup>1</sup>, Shin-Ming Huang<sup>3</sup>, Bahadur Singh<sup>4,5</sup>, Chuang-Han Hsu<sup>6</sup>, Tay-Rong Chang<sup>7</sup>, Jacob P. C. Ruff<sup>8</sup>, Kenji Watanabe<sup>9</sup>, Takashi Taniguchi<sup>9</sup>, Hsin Lin<sup>10</sup>, Goran Karapetrov<sup>11,12</sup>, Di Xiao<sup>2</sup>, Pablo Jarillo-Herrero<sup>1,12</sup> & Nuh Gedik<sup>1,12</sup>

Chirality is ubiquitous in nature, and populations of opposite chiralities are surprisingly asymmetric at fundamental levels<sup>1,2</sup>. Examples range from parity violation in the subatomic weak force to homochirality in biomolecules. The ability to achieve chirality-selective synthesis (chiral induction) is of great importance in stereochemistry, molecular biology and pharmacology<sup>2</sup>. In condensed matter physics, a crystalline electronic system is geometrically chiral when it lacks mirror planes, space-inversion centres or rotoinversion axes<sup>1</sup>. Typically, geometrical chirality is predefined by the chiral lattice structure of a material, which is fixed on formation of the crystal. By contrast, in materials with gyrotropic order<sup>3–6</sup>, electrons spontaneously organize themselves to exhibit macroscopic chirality in an originally achiral lattice. Although such order—which has been proposed as the quantum analogue of cholesteric liquid crystals—has attracted considerable interest<sup>3–15</sup>, no clear observation or manipulation of gyrotropic order has been achieved so far. Here we report the realization of optical chiral induction and the observation of a gyrotropically ordered phase in the transition-metal dichalcogenide semimetal 1T-TiSe<sub>2</sub>. We show that shining mid-infrared circularly polarized light on 1T-TiSe<sub>2</sub> while cooling it below the critical temperature leads to the preferential formation of one chiral domain. The chirality of this state is confirmed by the measurement of an out-of-plane circular photogalvanic current, the direction of which depends on the optical induction. Although the role of domain walls requires further investigation with local probes, the methodology demonstrated here can be applied to realize and control chiral electronic phases in other quantum materials<sup>4,16</sup>.

In the presence of strong correlations, the behaviour of electrons in a metal can deviate considerably from that of a weakly interacting Fermi gas, forming a wide range of complex, broken symmetry phases<sup>17</sup>. Recent theoretical works have highlighted the analogy between metallic electron systems and classical liquids<sup>17</sup>, in which a rich set of liquid-crystalline phases with varying degrees of symmetry breaking and transport properties have been observed. A well studied case is the nematic order<sup>17</sup>, that is, the spontaneous emergence of rotational anisotropy. In classical liquids, this is known as the nematic liquid-crystal phase, whereas it has recently been observed in several quantum systems<sup>17</sup>, including ruthenates, high-temperature superconductors, heavy-fermion superconductors and correlated metallic pyrochlores. Another fascinating case is the gyrotropic order, that is, the spontaneous emergence of geometrical chirality. In classical liquids, this is known

as the cholesteric liquid-crystal phase. Although gyrotropic order in quantum materials is of fundamental interest<sup>3–14</sup>, a clear observation of such order is still lacking.

For a condensed matter system, one route to obtain chirality is to look for low-symmetry materials that naturally crystalize in lattice structures that are free of mirror, inversion and rotoinversion symmetries—that is, chiral crystals. Representative chiral-crystal materials include quartz, tellurium, carbon nanotubes and twisted bilayer graphene. Another, highly unconventional, route is the gyrotropic order: an electronic system can spontaneously break the space-inversion, mirror-reflection and rotoinversion symmetries of the originally achiral lattice and, as a result, gain a definite chirality. Such a gyrotropic order<sup>3–6</sup> was suggested for 1T-TiSe<sub>2</sub><sup>7–9</sup> and copper oxides<sup>10</sup> on the basis of scanning tunnelling microscopy and polar Kerr rotation measurements. However,

<sup>1</sup>Department of Physics, Massachusetts Institute of Technology, Cambridge, MA, USA. <sup>2</sup>Department of Physics, Carnegie Mellon University, Pittsburgh, PA, USA. <sup>3</sup>Department of Physics, National Sun Yat-sen University, Kaohsiung, Taiwan. <sup>4</sup>SZU-NUS Collaborative Center and International Collaborative Laboratory of 2D Materials for Optoelectronic Science and Technology, Engineering Technology Research Center for 2D Materials Information Functional Devices and Systems of Guangdong Province, College of Optoelectronic Engineering, Shenzhen University, Shenzhen, China. <sup>5</sup>Department of Physics, Northeastern University, Boston, MA, USA. <sup>6</sup>Department of Electrical and Computer Engineering, National University of Singapore, Singapore, Singapore. <sup>7</sup>Department of Physics, National Cheng Kung University, Tainan, Taiwan. <sup>8</sup>CHESS, Cornell University, Ithaca, NY, USA. <sup>9</sup>National Institute for Materials Science, Tsukuba, Japan. <sup>10</sup>Institute of Physics, Academia Sinica, Taipei, Taiwan. <sup>11</sup>Department of Physics, Drexel University, Philadelphia, PA, USA. <sup>12</sup>Department of Materials Science and Engineering, Drexel University, Philadelphia, PA, USA. <sup>13</sup>These authors contributed equally: Su-Yang Xu, Qiong Ma, Yang Gao. ✉e-mail: [jarillo@mit.edu](mailto:jarillo@mit.edu); [gedik@mit.edu](mailto:gedik@mit.edu)

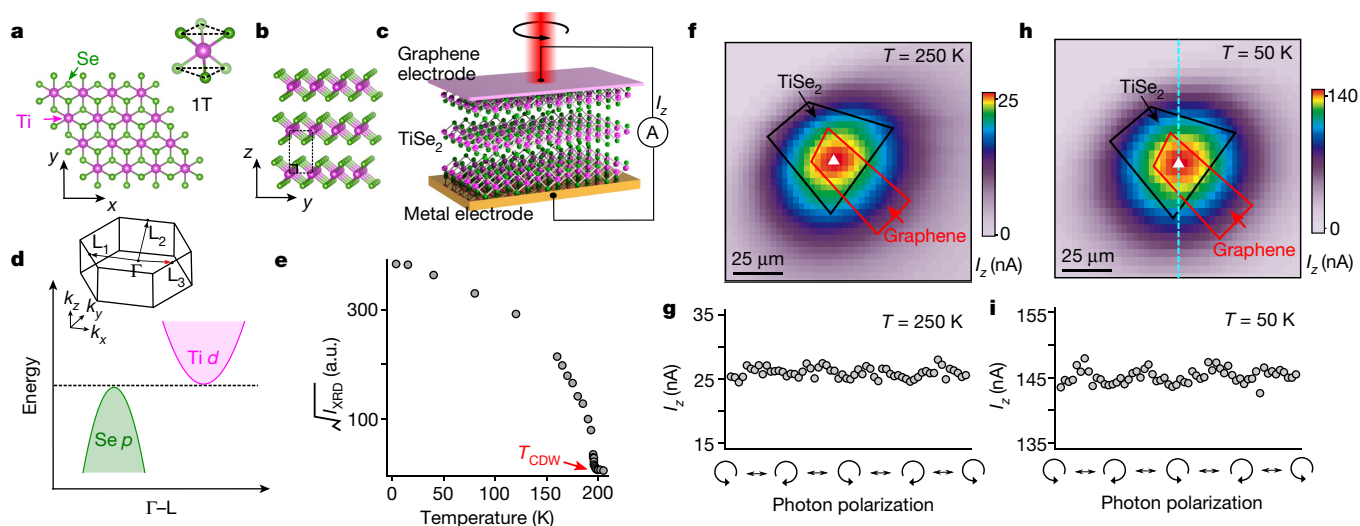


**Fig. 1 | Crystal structure and basic characterizations of 1T-TiSe<sub>2</sub>.** **a, b**, Crystal structure of 1T-TiSe<sub>2</sub>. The dashed triangles outline the triangular lattice, and the dashed square denotes the unit cell. **c**, Schematic illustration of our vertical photoactive devices. **d**, Schematic illustration of the normal-state bands of 1T-TiSe<sub>2</sub>. Inset, normal-state Brillouin zone.  $k_x$ ,  $k_y$ , and  $k_z$  are the principal directions of the reciprocal space.  $\Gamma$  and L are high-symmetry points of the reciprocal space. There are three inequivalent L points, denoted as L<sub>1</sub>, L<sub>2</sub> and L<sub>3</sub>. **e**, Square root of the X-ray diffraction (XRD) intensity peak of the superlattice

subsequent studies<sup>11,18,19</sup> indicated that the available experimental evidence was insufficient. Therefore, no conclusive experimental realization of gyrotropic order and the manipulation of the emergent chirality in these materials has been achieved so far. Theoretical studies have found that gyrotropic order can arise from a number of electronic instabilities, including chiral charge-density waves (CDWs)<sup>3–5</sup>, loop-current order<sup>12</sup>, odd-parity electronic (Pomeranchuk) instabilities<sup>6</sup> and electron–phonon-driven instabilities<sup>13</sup>. Moreover, because gyrotropic order must be odd under parity transformation, it may serve as a strong precursor for odd-parity Cooper pairing<sup>20</sup>, providing a mechanism for unconventional superconductivity<sup>4,5,12,14,20</sup>. In addition, it has been predicted that geometrical chirality can guarantee the existence of topological Weyl fermions<sup>21,22</sup>. Thus, the manipulation of emergent chirality in a gyrotropic phase may enable the realization of highly tunable Berry curvature and topological properties.

One challenge is to identify a clear experimental signature of geometrical chirality in metals. For insulating chiral crystals or molecules, chirality can be measured by optical activity<sup>5,15</sup>, which manifests as the rotation of the linear polarization plane as light travels through a nonmagnetic chiral medium. However, this is difficult in metallic bulk materials because they do not transmit light in bulk samples. Another challenge is to align chiral domains, because if they are not aligned the signal of the chirality probe will be cancelled by small domains of opposite chirality. In this work, we carefully addressed these challenges. Firstly, we identified a type of photocurrent as a unique signature of chirality in metallic electron systems. The circular photogalvanic effect (CPGE) generates a photocurrent, the direction of which depends on the chirality of light<sup>23</sup>. Here, we show that the out-of-plane CPGE current under normal incident light—that is, the CPGE current is parallel to the light-propagation direction—serves as a clear signature of the emergence of geometrical chirality in a metallic electron system<sup>22</sup>. Secondly, we realized a chirality-selective stimulus. We realize chiral induction of gyrotropic order using mid-infrared circularly polarized light.

The layered transition-metal dichalcogenide 1T-TiSe<sub>2</sub> (Fig. 1a, b) is a correlated semimetal, which has attracted great interest because of its

(Miller index (1/2, 1/2, 23/2) owing to the  $2 \times 2 \times 2$  CDW). The critical temperature of the CDW,  $T_{\text{CDW}}$ , is determined to be around 198 K. a.u., arbitrary units. **f**, Out-of-plane photocurrent  $I_z$  with linear polarization, measured as a function of the beam-spot location in real space at  $T = 250$  K. The black and red boxes trace the outline of the TiSe<sub>2</sub> flake and the graphene flake, respectively. **g**,  $I_z$  as a function of light polarization, with the beam spot fixed near the device centre (white triangle in **f**) at  $T = 250$  K. **h, i**, As in **f, g** but at  $T = 50$  K.

rich variety of unusual electronic properties<sup>24–30</sup>. It undergoes a commensurate CDW transition at a temperature of  $T_{\text{CDW}} \approx 200$  K, leading to a simple  $(2 \times 2 \times 2)$  superlattice<sup>31</sup> (Fig. 1a, b). Its vanishing, indirect bandgap (Fig. 1d)<sup>24,26,27</sup>, low carrier concentration and strong Coulomb interactions create optimal conditions for excitonic condensation<sup>30</sup>. Moreover, superconductivity and incommensurate CDWs emerge through chemical doping<sup>25</sup> in the bulk and by electrostatic gating in ultra-thin flakes<sup>29</sup>. Recently, a truly two-dimensional CDW has been observed<sup>28</sup> in monolayer TiSe<sub>2</sub>.

Here, we study the mid-infrared (wavelength of  $\lambda = 10.6$   $\mu\text{m}$ ; energy of  $\hbar\omega = 117$  meV;  $\hbar$ , reduced Planck constant;  $\omega$ , frequency) photocurrent response of TiSe<sub>2</sub> flakes (thickness of  $\sim 200$  nm, comparable to the laser skin depth<sup>26</sup>; see Methods for details of the experimental setups. Figure 1f presents the spatial map of the photocurrent  $I_z$  at a temperature of  $T = 250$  K—that is,  $I_z$  as a function of the beam-spot location in real space. Figure 1g shows the polarization dependence of  $I_z$ , with the beam-spot fixed at the sample centre. These data reveal a polarization-independent  $I_z$  signal that roughly spans the entire area of the TiSe<sub>2</sub> sample. We identify this signal as the regularly observed photothermoelectric current<sup>23</sup>. Lowering the temperature ( $T = 50$  K in Fig. 1h, i) gives qualitatively similar results, except that the magnitude of this polarization-independent photothermoelectric signal increases. For the datasets presented in this figure, the sample was cooled down without laser illumination.

We now shine circularly polarized light on the sample during the entire cooling process. As shown in Fig. 2a, we shine left circularly polarized (LCP) light on the sample while lowering its temperature from  $T = 250$  K. When a low temperature ( $T = 50$  K) is reached, we turn off this ‘induction light’. By measuring  $I_z$  as a function of polarization with the beam spot fixed at the sample centre (Fig. 2c), we measure a clear out-of-plane CPGE photocurrent, which is observed as long as the beam spot is on the sample (Fig. 2c). By increasing the temperature step by step, we observe (Fig. 2d) that the CPGE persists up to 170 K and then vanishes abruptly. In contrast, as expected, the polarization-independent photothermoelectric signal evolves smoothly with increasing temperature

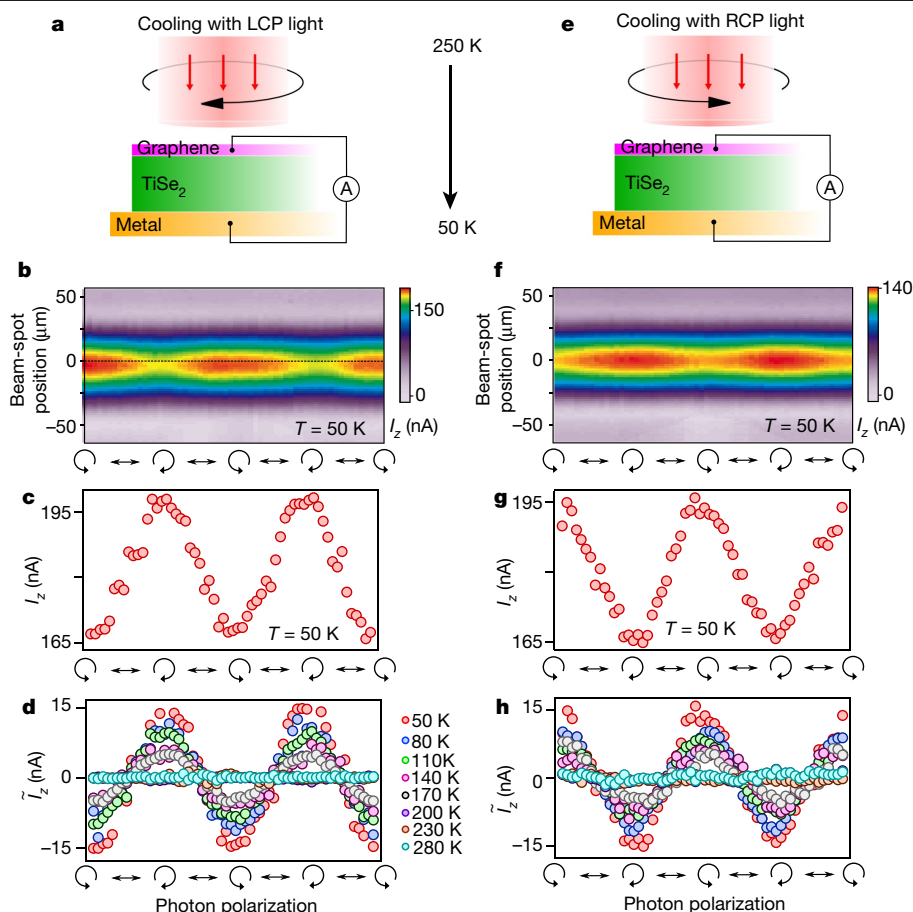


**Fig. 2 | Observation of an emergent out-of-plane circular photogalvanic current upon chiral induction.** **a**, We shine LCP light on the sample while lowering its temperature from  $T = 250$  K to 50 K. **b**, Out-of-plane photocurrent  $I_z$  at  $T = 50$  K as a function of light polarization (horizontal axis) and beam-spot location (vertical axis). The trajectory of the beam-spot position is denoted by

the blue dashed line in Fig. 1h. **c**,  $I_z$  at  $T = 50$  K as a function of polarization. **d**, The polarization-dependent (CPGE) part of  $I_z$ ,  $\tilde{I}_z$ , at different temperatures, during heating of the sample from 50 K to room temperature. The polarization-independent part of  $I_z$  for this dataset is presented in Extended Data Fig. 1. **e–h**, As in **a–d**, but for LCP-light illumination.

and remains finite up to 280 K (Extended Data Fig. 1). These sharply different dependences on temperature and on circularly polarized illumination during cooling further distinguish the CPGE photocurrent from the photothermoelectric signal (see Supplementary Information sections I, III). We repeat the measurements described above but change the light polarization during cooling to left circularly polarized (RCP) (Fig. 2e–h). The sign of the out-of-plane CPGE photocurrent is reversed (Fig. 2f–h), whereas other behaviours, such as the temperature dependence (Fig. 2h) and the spatial distribution (Fig. 2f) of  $I_z$ , are qualitatively similar. We find that the CPGE photocurrent is stable over time as long as temperature is lower than a critical temperature  $T_{\text{gyro}} \approx 174$  K (discussed in detail later).

We now establish the connection between the out-of-plane CPGE photocurrent and geometrical chirality. Here we adopt an intuitive physical picture that focuses only on the mirror symmetry, and we provide the details of the mathematical analysis of all relevant symmetries in Supplementary Information section II. Starting from a mirror-symmetric, achiral system, we assume that shining LCP light leads to an out-of-plane photocurrent  $I_z$  parallel to the light-propagation direction (Fig. 3a). We then perform a mirror transformation on the entire experiment (Fig. 3a). Under mirror reflection, LCP light changes to RCP light, the mirror-symmetric, achiral crystal remains invariant, and  $I_z$  (a vector parallel to the mirror plane) also remains invariant. Therefore,  $I_z$  is identical under LCP and RCP light for a mirror-symmetric, achiral crystal (Fig. 3a). In other words, the out-of-plane CPGE photocurrent ( $I_z^{\text{CPGE}} = I_z^{\text{RCP}} - I_z^{\text{LCP}}$ ) is forbidden by the mirror sym-

metry of the crystal. By contrast, if the crystal is chiral, a mirror transformation flips the chirality of both the crystal and the light simultaneously. Therefore, the mirror symmetry alone forces the photocurrent  $I_z$  under LCP light in a left-handed crystal to be identical to  $I_z$  under RCP light in a right-handed crystal (Fig. 3b). By contrast, for a crystal with fixed chirality, there is no symmetry that can relate  $I_z^{\text{RCP}}$  to  $I_z^{\text{LCP}}$ . Therefore, the out-of-plane CPGE photocurrent uniquely corresponds to geometrical chirality. In Supplementary Information section III we discuss systematically how extrinsic origins for the CPGE can be excluded.

We further study the out-of-plane CPGE photocurrent  $I_z^{\text{CPGE}}$  as a function of temperature and laser power. After cooling the system to  $T = 150$  K with LCP light, we measure  $I_z^{\text{CPGE}}$  at small temperature increments. The results (Fig. 3c) reveal the critical temperature ( $T_{\text{gyro}}$ ) for the onset of geometrical chirality. For all samples tested, we find  $T_{\text{gyro}} \approx 174$  K. We then study the dependence of  $I_z^{\text{CPGE}}$  on laser power. As shown in Fig. 3d, we fix the induction power (the laser power used for chiral induction) and measure  $I_z^{\text{CPGE}}$  as a function of the detection power (the laser power used to measure the CPGE photocurrent) at various temperatures. At temperatures much lower than  $T_{\text{gyro}}$ ,  $I_z^{\text{CPGE}}$  depends linearly on the detection power, whereas near  $T_{\text{gyro}}$ ,  $I_z^{\text{CPGE}}$  shows a non-monotonic pattern. With increasing detection power,  $I_z^{\text{CPGE}}$  first increases and then decreases. Then, we fix the detection power and measure  $I_z^{\text{CPGE}}$  as a function of the induction power at  $T = 100$  K (Fig. 3e). The results show that  $I_z^{\text{CPGE}}$  grows approximately linearly with induction power.



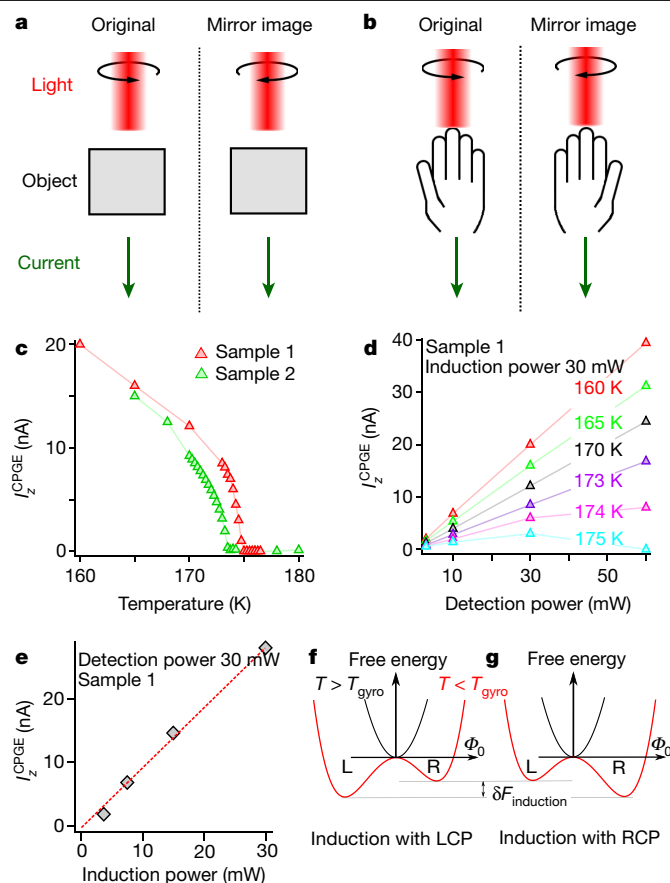


**Fig. 3 | Dependence of chiral induction and spontaneously emergent gyrotropic order on the temperature and laser power.** **a, b,** Illustration showing the connection between the out-of-plane CPGE photocurrent and the geometric chirality. **c,** CPGE photocurrent,  $I_{CPGE}^z$ , measured at small temperature increments, after cooling the sample to  $T = 150$  K using LCP light. **d,** Measured  $I_{CPGE}^z$  as a function of detection power at various temperatures for fixed induction power. Lines in **c, d** are guides to the eye. **e,** Measured  $I_{CPGE}^z$  as a function of induction power at  $T = 100$  K for fixed detection power. Squares are data points and the red dotted line is a linear fit. **f, g,** Schematic illustration of the free energy as a function of the order parameter  $\Phi_0$  (see main text).

Regarding the possible physical origins of the observed onset temperature, we propose that  $T_{gyro}$  may represent the onset temperature of the gyrotropic phase or the temperature at which chiral domains thermally evolve into domain sizes smaller than the spot size. We measured the dependence of  $T_{gyro}$  on the training power (the laser power used for the optical induction). Our data (Supplementary Information section I) do not show substantial variation of the onset temperature at different training powers, which suggests that  $T_{gyro}$  represents the onset temperature of the gyrotropic phase. To estimate the temperature increase due to the detection light, we measured the dependence of  $T_{gyro}$  on the detection power. Our data (Supplementary Information section I) show a temperature increase of less than 1 K for the largest detection power, which is consistent with the independent estimation of this temperature increase from photothermoelectric signals (Extended Data Fig. 1). Further, we measured the temperature-dependent CPGE photocurrent in a full thermal cycle, and our data do not show observable hysteresis (Supplementary Information section I). In Supplementary Information section I and Extended Data Fig. 2, we present measurements on another type of device that can detect both the in-plane and out-of-plane photocurrents independently, which confirm the observation of the out-of-plane CPGE photocurrent and the chiral induction. In Supplementary Information section IX, we show

that the cross-talk between the in-plane and out-of-plane currents is negligibly small according to the aspect ratio of our current devices.

Finally, we discuss how our data uncover the physics of the gyrotropic-phase transition and chiral induction in 1T-TiSe<sub>2</sub>. Our analysis shows that chiral induction can be achieved by shining circularly polarized light while cooling to temperatures below  $T_{gyro}$ . However, directly applying circularly polarized light at low temperatures cannot reverse the emergent chirality (for laser powers within our experimental capability). This shows that, as expected, at low temperatures the chiral domains become much stiffer than near  $T_{gyro}$ . This is further supported by the observed detection-power dependence of  $T_{gyro}$  shown in Fig. 3d: the linear detection-power profile at low temperatures agrees with the second-order optoelectronic nature of CPGE (that is, the second-order dependence of the CPGE photocurrent on the electric field of light.). Alternatively, the non-monotonic profile near  $T_{gyro}$  may indicate that the chiral domains are partially reversed by the detection light.

We analyse our observations within the framework of the Landau phase-transition theory, paying particular attention to the broken symmetries. Generally, the order parameter for a gyrotropic-phase transition can be expressed as  $\Phi_{gyro} = \Phi_0(T)f(\mathbf{r})$ , where  $f(\mathbf{r})$  is odd under the inversion, mirror and rotoinversion symmetries, and  $\Phi_0(T)$  is a real number with a value that depends on temperature. As the temperature is lowered across  $T_{gyro}$ ,  $\Phi_0$  becomes non-zero, breaking the inversion, mirror and rotoinversion symmetries of the system.  $\Phi_0 < 0$  and  $\Phi_0 > 0$  correspond to the left and right chiral domains, which are energetically degenerate in the absence of optical chiral induction. We now aim to identify the appropriate form for the coupling between circularly polarized light and the chiral domains (denoted as  $\delta F_{induction}$ ). The circularly polarized light is characterized by its time-dependent, spatially rotating electric field  $\mathbf{E}$ . Because  $\delta F_{induction}$  must be time-independent, it cannot be linearly proportional to  $\mathbf{E}$ . We performed systematic symmetry analyses based on our experimental observations (Supplementary Information section V), and we determined  $\delta F_{induction}$  to the lowest order of the electric field of light to have the form  $\delta F_{induction} = \Phi_{gyro} \left[ \left( \mathbf{E} \times \frac{\partial \mathbf{E}}{\partial z} \right) \cdot \hat{\mathbf{z}} \right]$ , where  $\mathbf{E} = |\mathbf{E}| \left[ \cos\left(\frac{2\pi}{\lambda}z - \omega t\right) \hat{\mathbf{x}} \pm \sin\left(\frac{2\pi}{\lambda}z - \omega t\right) \hat{\mathbf{y}} \right]$ . We confirm that  $\left( \mathbf{E} \times \frac{\partial \mathbf{E}}{\partial z} \right) \cdot \hat{\mathbf{z}}$  is time-independent and flips sign as the light chirality is reversed.

Moreover,  $\left( \mathbf{E} \times \frac{\partial \mathbf{E}}{\partial z} \right) \cdot \hat{\mathbf{z}}$  is odd under any mirror reflection, space inversion and rotoinversion. Therefore,  $\delta F_{induction} = \Phi_{gyro} \left[ \left( \mathbf{E} \times \frac{\partial \mathbf{E}}{\partial z} \right) \cdot \hat{\mathbf{z}} \right]$  is totally symmetric and transforms as a scalar. We verify that this form of  $\delta F_{induction}$  tilts the total free-energy landscape in opposite ways depending on light chirality (Fig. 3f, g). Furthermore, the coupling term  $\delta F_{induction}$  suggests a linear dependence on the optical induction power ( $\delta F_{induction} \propto E^2$ ), which is consistent with our observation of the CPGE signal being linearly proportional to the induction power. In Supplementary Information section VII, we describe a microscopic theoretical interpretation of the chiral induction. We show that the chiral induction arises from optical activity. Interestingly, the optical activity is symmetric under time reversal. In sharp contrast, the effects that enable circularly polarized light to manipulate magnetism (for example, the inverse Faraday effect)<sup>32</sup> require the breaking of time-reversal symmetry. This discrepancy highlights the difference between the chiral induction observed here and studies using light to manipulate magnetism<sup>32</sup>. In Methods, we describe further analysis of the gyrotropic order using a microscopic picture of chiral CDWs<sup>3</sup>.

Looking forward, important open questions remain, calling for future studies. For instance, the role of domain walls has not been directly determined, owing to the lack of nanometre-scale spatial resolution. It is possible that domain walls can also be manipulated by circularly polarized light and contribute to the CPGE, although we expect their contribution to be considerably smaller than that of the bulk (Supplementary Information section III).

Our measurements and analyses clearly demonstrate gyrotropic order and chiral induction, paving the way to exciting experimental possibilities. We establish the mid-infrared CPGE photocurrent as a powerful probe for broken-symmetry states in metals. In particular, the mid-infrared photon energy corresponds to relevant energy scales in correlated systems, such as the CDW gap in  $\text{TiSe}_2$  and the pseudo-gap in copper oxides. Furthermore, the second-order nature of the CPGE is uniquely sensitive to odd-parity order parameters<sup>6</sup>. Therefore, the mid-infrared CPGE may provide new insights into other important problems in quantum materials, such as the pseudo-gap state of copper oxides and the newly observed insulating and superconducting orders in ‘magic-angle’ twisted bilayer graphene<sup>33</sup>.

## Online content

Any methods, additional references, Nature Research reporting summaries, source data, extended data, supplementary information, acknowledgements, peer review information; details of author contributions and competing interests; and statements of data and code availability are available at <https://doi.org/10.1038/s41586-020-2011-8>.

- Wagnière, G. H. *On Chirality and the Universal Asymmetry: Reflections on Image and Mirror Image* (John Wiley & Sons, 2008).
- Feringa, B. L. & Van Delden, R. A. Absolute asymmetric synthesis: the origin, control, and amplification of chirality. *Angew. Chem. Int. Ed.* **38**, 3418–3438 (1999).
- van Wezel, J. Chirality and orbital order in charge density waves. *Europhys. Lett.* **96**, 67011 (2011).
- Hosur, P., Kapitulin, A., Kivelson, S., Orenstein, J. & Raghu, S. Kerr effect as evidence of gyrotropic order in the cuprates. *Phys. Rev. B* **87**, 115116 (2013).
- Orenstein, J. & Moore, J. E. Berry phase mechanism for optical gyrotropy in stripe-ordered cuprates. *Phys. Rev. B* **87**, 165110 (2013).
- Fu, L. Parity-breaking phases of spin–orbit-coupled metals with gyrotropic, ferroelectric, and multipolar orders. *Phys. Rev. Lett.* **115**, 026401 (2015).
- Ishioaka, J. et al. Chiral charge-density waves. *Phys. Rev. Lett.* **105**, 176401 (2010).
- Iavarone, M. et al. Evolution of the charge density wave state in  $\text{Cu}_x\text{TiSe}_2$ . *Phys. Rev. B* **85**, 155103 (2012).
- Castellan, J.-P. et al. Chiral phase transition in charge ordered 1T- $\text{TiSe}_2$ . *Phys. Rev. Lett.* **110**, 196404 (2013).
- Xia, J. et al. Polar Kerr-effect measurements of the high-temperature  $\text{YBa}_2\text{Cu}_3\text{O}_{6+x}$  superconductor: evidence for broken symmetry near the pseudogap temperature. *Phys. Rev. Lett.* **100**, 127002 (2008).
- Hildebrand, B. et al. Local real-space view of the achiral 1T- $\text{TiSe}_2$   $2 \times 2$  charge density wave. *Phys. Rev. Lett.* **120**, 136404 (2018).
- Varma, C. Gyrotropic birefringence in the underdoped cuprates. *Europhys. Lett.* **106**, 27001 (2014).
- Zenker, B., Fehske, H., Beck, H., Monney, C. & Bishop, A. Chiral charge order in 1T- $\text{TiSe}_2$ : importance of lattice degrees of freedom. *Phys. Rev. B Condens. Matter Mater. Phys.* **88**, 075138 (2013).
- Ganesh, R., Baskaran, G., van den Brink, J. & Efremov, D. V. Theoretical prediction of a time-reversal broken chiral superconducting phase driven by electronic correlations in a single  $\text{TiSe}_2$  layer. *Phys. Rev. Lett.* **113**, 177001 (2014).
- Gradhand, M. & van Wezel, J. Optical gyrotropy and the nonlocal Hall effect in chiral charge-ordered  $\text{TiSe}_2$ . *Phys. Rev. B* **92**, 041111 (2015).
- Sugawara, Y. et al. Incommensurate chiral CDW in 1T- $\text{VSe}_2$ . Preprint at <https://arxiv.org/abs/1812.01368> (2018).
- Fradkin, E., Kivelson, S. A., Lawler, M. J., Eisenstein, J. P. & Mackenzie, A. P. Nematic fermi fluids in condensed matter physics. *Annu. Rev. Condens. Matter Phys.* **1**, 153–178 (2010).
- Armitage, N. Constraints on Jones transmission matrices from time-reversal invariance and discrete spatial symmetries. *Phys. Rev. B* **90**, 035135 (2014).
- Hosur, P., Kapitulin, A., Kivelson, S., Orenstein, J. & Raghu, S. Kerr effect as evidence of gyrotropic order in the cuprates. *Phys. Rev. B* **91**, 039908 (2015).
- Kozii, V. & Fu, L. Odd-parity superconductivity in the vicinity of inversion symmetry breaking in spin–orbit-coupled systems. *Phys. Rev. Lett.* **115**, 207002 (2015).
- Chang, G. et al. Universal topological electronic properties of nonmagnetic chiral crystals. *Nat. Mater.* **17**, 978–985 (2018).
- de Juan, F., Grushin, A. G., Morimoto, T. & Moore, J. E. Quantized circular photogalvanic effect in Weyl semimetals. *Nat. Commun.* **8**, 15995 (2017).
- McIver, J., Hsieh, D., Steinberg, H., Jarillo-Herrero, P. & Gedik, N. Control over topological insulator photocurrents with light polarization. *Nat. Nanotechnol.* **7**, 96–100 (2012).
- Kidd, T., Miller, T., Chou, M. & Chiang, T.-C. Electron–hole coupling and the charge density wave transition in  $\text{TiSe}_2$ . *Phys. Rev. Lett.* **88**, 226402 (2002).
- Morosan, E. et al. Superconductivity in  $\text{Cu}_x\text{TiSe}_2$ . *Nat. Phys.* **2**, 544–550 (2006).
- Li, G. et al. Semimetal-to-semimetal charge density wave transition in 1T- $\text{TiSe}_2$ . *Phys. Rev. Lett.* **99**, 027404 (2007).
- Porer, M. et al. Non-thermal separation of electronic and structural orders in a persisting charge density wave. *Nat. Mater.* **13**, 857–861 (2014).
- Chen, P. et al. Charge density wave transition in single-layer titanium diselenide. *Nat. Commun.* **6**, 8943 (2015).
- Li, L. et al. Controlling many-body states by the electric-field effect in a two-dimensional material. *Nature* **529**, 185–189 (2016).
- Kogar, A. et al. Signatures of exciton condensation in a transition metal dichalcogenide. *Science* **358**, 1314–1317 (2017).
- Holt, M., Zschack, P., Hong, H., Chou, M. & Chiang, T.-C. X-ray studies of phonon softening in  $\text{TiSe}_2$ . *Phys. Rev. Lett.* **86**, 3799 (2001).
- Kirilyuk, A., Kimel, A. V. & Rasing, T. Ultrafast optical manipulation of magnetic order. *Rev. Mod. Phys.* **82**, 2731–2784 (2010).
- Cao, Y. et al. Unconventional superconductivity in magic-angle graphene superlattices. *Nature* **556**, 43–50 (2018).

**Publisher's note** Springer Nature remains neutral with regard to jurisdictional claims in published maps and institutional affiliations.

© The Author(s), under exclusive licence to Springer Nature Limited 2020

### Sample fabrication

To probe the out-of-plane photocurrent  $I_z$ , we fabricated vertical photoactive devices consisting of a TiSe<sub>2</sub> flake sandwiched between a transparent graphene electrode at the top and a metal electrode at the bottom (Fig. 1c). The thickness of the TiSe<sub>2</sub> flakes is comparable to the laser skin depth (~200 nm), which is calculated from the optical conductivity at  $\lambda = 10.6 \mu\text{m}$  (ref. <sup>26</sup>); this ensures that a sizeable vertical fraction of the flake is photoactive. First, the bottom metal (PdAu) contacts were deposited on standard Si/SiO<sub>2</sub> substrates. These substrates were then transferred into an argon-environment glovebox with water and oxygen levels of less than 0.1 ppm. TiSe<sub>2</sub> was exfoliated inside the glovebox, and flakes with a thickness of a few hundred nanometres were selected. A selected TiSe<sub>2</sub> flake was first picked up by a poly(bisphenol A carbonate) stamp and directly transferred onto the substrate. The poly(bisphenol A carbonate) was then dissolved. Subsequently, hexagonal boron nitride (h-BN), graphene and h-BN flakes were picked up one by one, and the whole stack was then placed on top of the TiSe<sub>2</sub> flake. The graphene served as a transparent top electrode and touched the side electrode for wire bonding. The lower h-BN layer worked as the edge spacer between the top-electrode graphene and the bottom metal. The top h-BN layer covered the active area (the overlapping area between the top graphene layer, the TiSe<sub>2</sub> and the bottom contact) to prevent the device from degradation.

X-ray diffraction measurements were performed at the Cornell High Energy Synchrotron Source (CHESS) A2 beamline, using 38.5-keV photons. The incident photon energy was selected using a perfect high-pressure high-temperature diamond (111) double-crystal monochromator, with a narrow incident bandwidth of less than  $e^{-4}$ . The height and width of the incident beam on the sample was ~150  $\mu\text{m}$  and ~600  $\mu\text{m}$ , respectively. The crystal was mounted on a temperature-controlled copper post inside a closed-cycle cryostat, with temperature stability better than  $\pm 0.1$  K and absolute temperature calibration better than 1 K. The CDW peak intensities were collected using a four-circle diffractometer and a high-dynamic-range photon-counting area detector.

### Mid-infrared scanning photocurrent microscopy

Our experimental setup includes a mid-infrared scanning photocurrent microscope, which allows us to measure the mid-infrared photocurrent as a function of beam-spot location, light polarization and temperature (Fig. 1c). The laser source is a temperature-stabilized CO<sub>2</sub> laser ( $\lambda = 10.6 \mu\text{m}$  or  $\hbar\omega = 117$  meV). A focused beam spot (beam waist ~25  $\mu\text{m}$ ) is scanned (using a two-axis piezo-controlled scanning mirror) over the entire sample and the current is recorded at the same time to form a two-dimensional map of the photocurrent as a function of the beam-spot position. Light reflected from the sample is collected to form a simultaneous reflection image of the sample. The absolute location of the photoinduced signal is therefore found by comparing the photocurrent map to the reflection image. The light polarization is modulated by rotating a quarter-wave plate. The CPGE is an intrinsic photocurrent response<sup>34–36</sup>. As a second-order effect, the CPGE current depends quadratically on the electric field of the light (the light used to measure the CPGE). The in-plane CPGE current under oblique or normal light incidence has been studied in a wide range of materials<sup>22,23,37–45</sup>. Any intrinsic CPGE requires the material to break inversion symmetry<sup>22,23,34–45</sup>. The out-of-plane CPGE photocurrent under normal incidence serves as a signature of geometrical chirality (Supplementary Information section II).

We further analyse the microscopic nature of the gyrotropic order. One likely mechanism is chiral CDWs<sup>3</sup> (Supplementary Information section VI): on each layer, one of the three CDWs has the dominant amplitude and, as one travels from one layer to the next along the out-of-plane direction, the dominant direction rotates in a chiral way. Indeed, it has been theoretically predicted<sup>3</sup> that if the chiral CDW phase

does exist, then TiSe<sub>2</sub> would need to first enter the normal CDW phase and then go into the chiral CDW phase at a slightly lower temperature, consistent with our observations here. Within this microscopic picture, the free energy can be expressed as

$$F = F_{\text{CDW}} + F_{\text{induction}} \quad (1)$$

$$F_{\text{CDW}} = \text{Re} \int d\mathbf{r} \left[ a(r)\rho^2 + b(r)\rho^3 + c(r)\rho^4 + d(r) \left( |\rho_1\rho_2|^2 + |\rho_2\rho_3|^2 + |\rho_3\rho_1|^2 \right) \right] \quad (2)$$

$$F_{\text{induction}} = \int d\mathbf{r} \theta(\rho, \rho^*; r) \left[ \mathbf{i}(\nabla\rho \times \nabla\rho^*) \cdot \hat{\mathbf{z}} \right] \left[ \mathbf{i} \left( \mathbf{E} \times \frac{\partial \mathbf{E}}{\partial z} \right) \right] \quad (3)$$

where  $\rho = \rho_1 + \rho_2 + \rho_3$  represents the modulations to the charge density due to the formation of the CDWs ( $\Gamma$  to  $L_1$ ,  $L_2$  and  $L_3$ , corresponding to  $\rho_1$ ,  $\rho_2$ ,  $\rho_3$ , respectively),  $a$ ,  $b$ ,  $c$  and  $d$  are appropriate coefficients that should reflect the symmetry of the lattice, and  $\theta$  consists of polynomials of  $\rho$  and  $\rho^*$  (see details in Supplementary Information section VI). As shown in ref. <sup>3</sup>, the chirality is defined by how the phase of the CDWs winds as a function of height. The term  $F_{\text{induction}}$  in equation (4) describes how chiral induction is realized by the coupling between the chiral CDW and circularly polarized light, and allows us to compute the electronic structure of TiSe<sub>2</sub> in the gyrotropically ordered (chiral CDW) phase (Supplementary Information section VII). In combination with the microscopic theory developed for chiral induction and CPGE generation (Supplementary Information section VII), we computed the chiral induction and the CPGE tensors in the gyrotropic states of TiSe<sub>2</sub> and compared them with our experimental data (Supplementary Information section VII).

### Data availability

The data that support the plots within this paper and other findings of this study are available from the corresponding author upon reasonable request. Some datasets are available at the Materials Data Facility at <https://doi.org/10.18126/r4sn-m7sa>.

34. Sipe, J. & Shkrebti, A. Second-order optical response in semiconductors. *Phys. Rev. B* **61**, 5337–5352 (2000).
35. Hosur, P. Circular photogalvanic effect on topological insulator surfaces: Berry-curvature-dependent response. *Phys. Rev. B* **83**, 035309 (2011).
36. Morimoto, T. & Nagaosa, N. Topological nature of nonlinear optical effects in solids. *Sci. Adv.* **2**, e1501524 (2016).
37. Olbrich, P. et al. Observation of the orbital circular photogalvanic effect. *Phys. Rev. B* **79**, 121302 (2009).
38. Ivchenko, E. & Ganichev, S. in *Spin Physics in Semiconductors* 245–277 (Springer, 2008).
39. Plank, H. & Ganichev, S. A review on terahertz photogalvanic spectroscopy of Bi<sub>2</sub>Te<sub>3</sub>- and Sb<sub>2</sub>Te<sub>3</sub>-based three dimensional topological insulators. *Solid-State Electron.* **147**, 44–50 (2018).
40. Yuan, H. et al. Generation and electric control of spin-valley-coupled circular photogalvanic current in WSe<sub>2</sub>. *Nat. Nanotechnol.* **9**, 851–857 (2014).
41. Dhara, S., Mele, E. J. & Agarwal, R. Voltage-tunable circular photogalvanic effect in silicon nanowires. *Science* **349**, 726–729 (2015).
42. Ma, Q. et al. Direct optical detection of Weyl fermion chirality in a topological semimetal. *Nat. Phys.* **13**, 842–847 (2017).
43. Lim, S., Rajamathi, C. R., Süß, V., Felser, C. & Kapitulnik, A. Temperature-induced inversion of the spin-photogalvanic effect in WTe<sub>2</sub> and MoTe<sub>2</sub>. *Phys. Rev. B* **98**, 121301 (2018).
44. Ji, Z. et al. Spatially dispersive circular photogalvanic effect in a Weyl semimetal. *Nat. Mater.* **18**, 955–962 (2019).
45. Xu, S.-Y. et al. Electrically switchable Berry curvature dipole in the monolayer topological insulator WTe<sub>2</sub>. *Nat. Phys.* **14**, 900–906 (2018).
46. Lakhani, A. A., Jandl, S., Ayache, C. & Jay-Gerin, J.-P. Thermoelectric power of TiSe<sub>2</sub>-S<sub>x</sub> mixed crystals at low temperatures. *Phys. Rev. B Condens. Matter* **28**, 1978–1982 (1983).

**Acknowledgements** We thank X. Xu, V. Fatemi, E. J. Sie and S. Fang for discussions. N.G., S.-Y.X., A.K. and A.Z. acknowledge support from the US Department of Energy, Office of Science, Office of Basic Energy Sciences, DMSE (data taking and analysis) and the Gordon and

Betty Moore Foundation's EPIQS Initiative through grant GBMF4540 (manuscript writing). Work in P.J.-H. group was supported through AFOSR grant FA9550-16-1-0382 (fabrication and measurement), as well as through the Center for the Advancement of Topological Semimetals, an Energy Frontier Research Center funded by the US Department of Energy Office of Science, Office of Basic Energy Sciences, through the Ames Laboratory under contract DE-AC02-07CH11358 (data analysis), and the Gordon and Betty Moore Foundation's EPIQS Initiative through grant GBMF 4541 to P.J.-H. This work made use of the Materials Research Science and Engineering Center Shared Experimental Facilities supported by the National Science Foundation (NSF) (grant number DMR-0819762). The work at Drexel University was supported by NSF through grant number ECCS-1711015. Research conducted at CHESS is supported by the NSF via awards DMR-1332208 and DMR-1829070. Work at CMU was supported by the Department of Energy, Basic Energy Sciences, Materials Sciences and Engineering Division, through grant number DE-SC0012509. K.W. and T.T. acknowledge support from the Elemental Strategy Initiative conducted by MEXT, Japan, JSPS KAKENHI grant numbers JP18K19136 and CREST (JPMJCR15F3), JST. T.-R.C. was supported by the Young Scholar Fellowship Program of the Ministry of Science and Technology (MOST) in Taiwan, under a MOST grant for the Columbus Program MOST108-2636-M-006-002, National Cheng Kung University, Taiwan, and National Center for Theoretical Sciences, Taiwan. This work was supported partially by MOST, Taiwan, via grant MOST107-2627-E-006-001. This research was supported in part by a Higher Education Sprout Project, Ministry of Education from the Headquarters of University Advancement at National Cheng Kung University (NCKU). S.-M.H. acknowledges support by the Ministry of Science and Technology (MoST) in Taiwan under grant number 105-2112-M-110-

014-MY3. H.L. acknowledges Academia Sinica, Taiwan for support under Innovative Materials and Analysis Technology Exploration (AS-iMATE-107-11).

**Author contributions** N.G. and P.J.-H. supervised the project. S.-Y.X. and Q.M. conceived the experiment. S.-Y.X. and Q.M. performed photocurrent measurements and analysed the data. A.K., J.P.C.R., S.-Y.X. and Q.M. performed X-ray diffraction measurements. A.M.M.V., T.H.D., Q.M. and S.-Y.X. fabricated the devices. Y.G. and S.-Y.X. performed theoretical analysis under the supervision of D.X. C.-H.H., S.-M.H., B.S. and T.-R.C. performed density functional theory calculations under the supervision of H.L. G.K. grew  $\text{TiSe}_2$  crystals. K.W. and T.T. grew the bulk h-BN single crystals. A.Z. made significant contributions to the symmetry analysis and the overall presentation. S.-Y.X., Q.M., P.J.-H. and N.G. wrote the manuscript with input from all authors.

**Competing interests** The authors declare no competing interests.

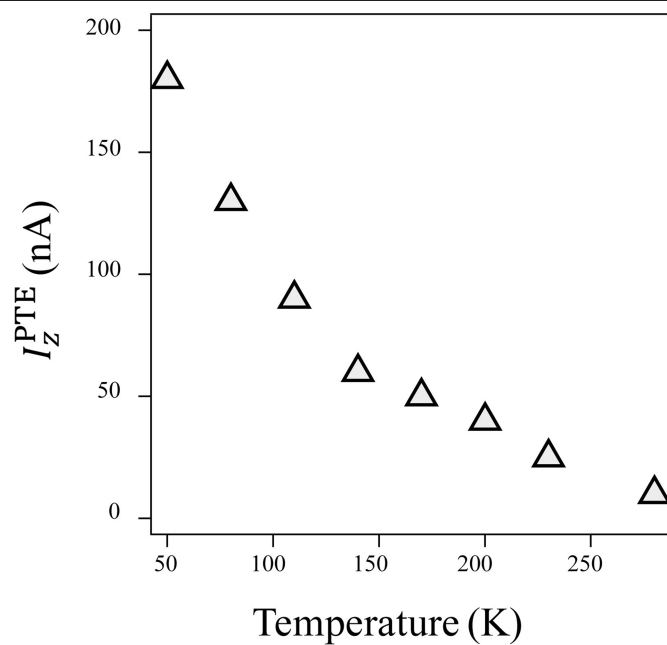
#### Additional information

**Supplementary information** is available for this paper at <https://doi.org/10.1038/s41586-020-2011-8>.

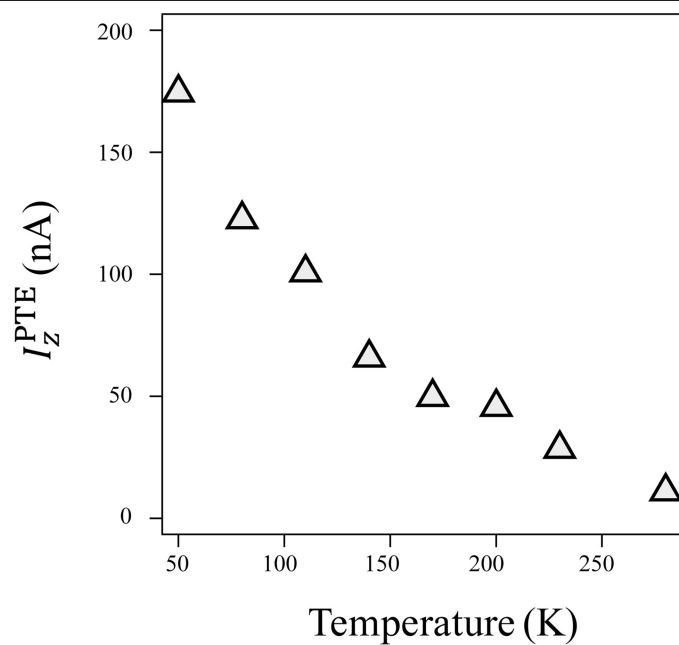
**Correspondence and requests for materials** should be addressed to P.J.-H. or N.G.

**Peer review information** *Nature* thanks Sajal Dhara, Jasper van Wezel and the other, anonymous, reviewer(s) for their contribution to the peer review of this work.

**Reprints and permissions information** is available at <http://www.nature.com/reprints>.

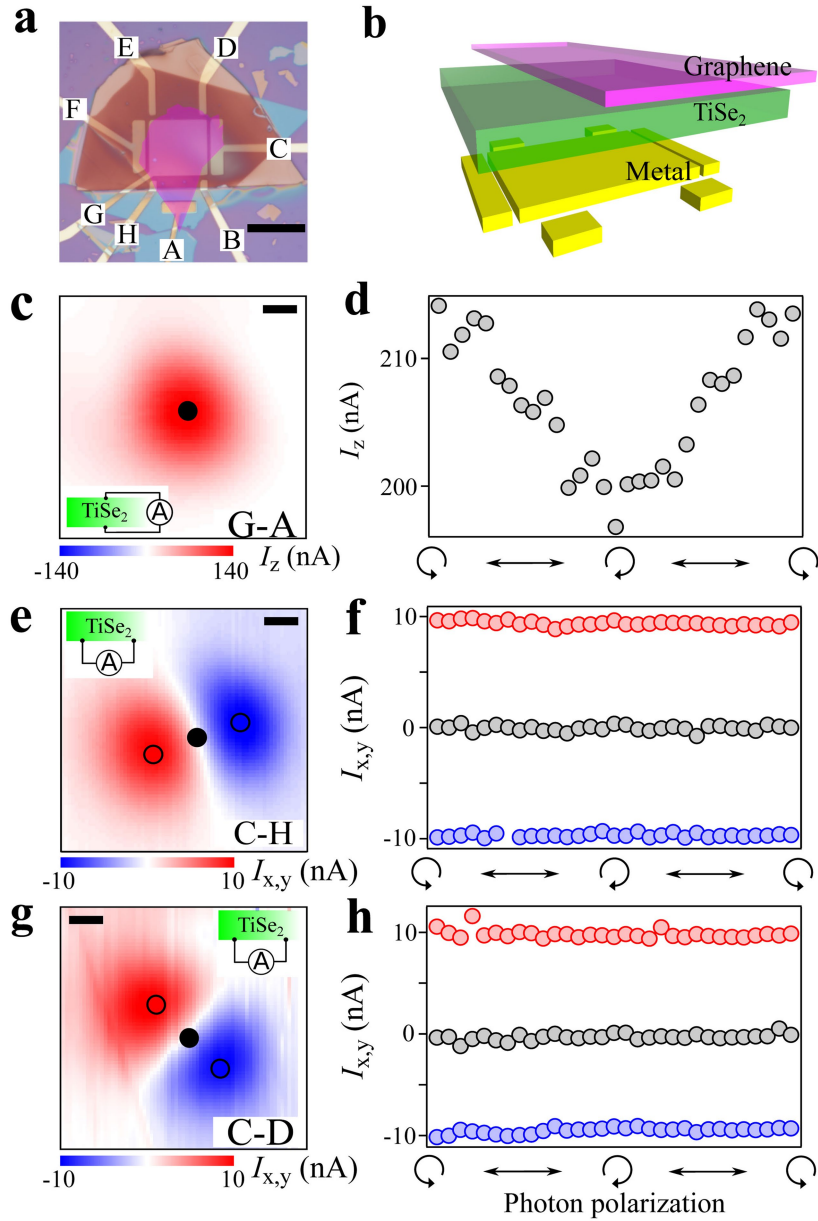


**Extended Data Fig. 1 | Polarization-independent photocurrent.** Measured photothermoelectric (PTE) current  $I_z^{\text{PTE}}$  at different temperatures during heating of the sample from 50 K to room temperature. The data shown here are from the same photocurrent measurements as those in Fig. 2d, h; they represent the polarization-independent component, whereas those in Fig. 2d,



h are the polarization-dependent component of the photocurrent. PTE currents of about 10 nA, 40 nA and 150 nA at 250 K, 170 K and 50 K correspond to a temperature increase of about 2 K, 0.5 K and 0.1 K at 50 K, 170 K and 250 K, respectively, according to the thermopower values measured in ref.<sup>46</sup>.





**Extended Data Fig. 2 | Contrasting behaviours of in-plane and out-of-plane photocurrents as a result of the gyrotropic order in 1T-TiSe<sub>2</sub>.** **a, b**, Optical image (**a**) and schematic illustration (**b**) of a TiSe<sub>2</sub> photoactive device that can detect both the in-plane and out-of-plane photocurrents independently. The electrodes are labelled by capital letters. **c**, Spatial map of the out-of-plane photocurrent  $I_z$  between electrodes G-A at  $T=100$  K. **d**, Polarization-dependent  $I_z$  data at  $T=100$  K. The measured photocurrent  $I_z$  is consistent with the results of previous devices (Figs. 2, 3). A single peak is observed in **c** that roughly covers the device. This peak consists of two independent signals: the polarization-independent background, which arises from the photothermoelectric effect and exists at all temperatures, and the

polarization-dependent CPGE signal (**d**), which depends on chiral induction and appears only at low temperatures. **e-h**, Same as **c, d**, but for the in-plane photocurrent  $I_{x,y}$  between electrodes C-H (**e, f**) and C-D (**g, h**).  $I_{x,y}$  shows distinctly different properties from  $I_z$ . No in-plane CPGE is observed (**f, h**). The polarization-independent signal shows a bipolar spatial configuration (**e, g**):  $I_{x,y}$  changes sign as the beam spot is scanned from one contact to the other. This bipolar spatial configuration, which has been widely observed in other in-plane photocurrent studies<sup>23</sup>, further confirms that the polarization-independent signals are photothermoelectric currents at the contact-sample junctions. Scale bars, 25  $\mu\text{m}$ . All data in this figure were collected after RCP chiral induction with an induction power of 30 mW.